Electrostatic built-in fields in wurtzite III-N nanostructures: Impact of growth plane on second-order piezoelectricity

Saroj K. Patra[1,2] and Stefan Schulz[1]
[1]*Photonics Theory Group, Tyndall National Institute, Dyke Parade, Cork T12R5CP, Ireland*
[2]*Department of Electrical Engineering, University College Cork, Cork T12YN60, Ireland*
(Received 14 August 2017; revised manuscript received 9 October 2017; published 20 October 2017)

In this work we present a detailed analysis of the second-order piezoelectric effect in wurtzite III-N heterostructures, such as quantum wells and quantum dots, grown on different substrate orientations. Our analysis is based on a continuum model using a here derived analytic expression for the second-order piezoelectric polarization vector field as a function of the incline angle θ to the wurtzite c axis. This expression allows for a straightforward implementation in existing quantum well and quantum dot codes. Our calculations on III-N quantum well systems reveal that especially for semipolar structures with high incline angle values ($55^\circ \leqslant \theta \leqslant 80^\circ$ and $105^\circ \leqslant \theta \leqslant 120^\circ$), second-order piezoelectricity noticeably contributes to the overall electric built-in field. For instance, in an InGaN/GaN multiple quantum well system with 22% In, the electric field increases by approximately 20% due to second-order piezoelectricity. Overall, when including second-order piezoelectric effects in the calculation of electric fields in GaN/AlN and InGaN/GaN quantum well systems an improved agreement between our theory and experimental literature data is observed. When studying quantum dots, at least for the here considered model geometry and growth planes, we observe that for GaN/AlN structures second-order effects are of secondary importance. The situation is different for non-c-plane $In_{0.2}Ga_{0.8}N$/GaN quantum dots. For example, inside a nonpolar $In_{0.2}Ga_{0.8}N$/GaN dot the built-in potential arising from second-order piezoelectricity is comparable in magnitude to the built-in potential originating from spontaneous and first-order piezoelectric polarization, but opposite in sign. This feature leads to a change in the built-in potential profile both in and around the $In_{0.2}Ga_{0.8}N$/GaN quantum dot structure, which in general is relevant for electronic and optical properties of these systems.

DOI: 10.1103/PhysRevB.96.155307

I. INTRODUCTION

Over recent years, electric polarization effects in semiconductors and related nanostructures have received significant research attention around the world [1–16]. This ranges from understanding fundamental electric polarization properties in different materials [1,2,4,6–8,10–12,14,15] to the connected impact on electronic and optical properties of heterostructures, which is important for designing novel devices [3,9,13,16]. In general the magnitude of the electric polarization effect strongly varies between different material systems and is tightly linked to their underlying crystal structure and features such as bond ionicity [1,2,15]. For instance Bernardini, Fiorentini, and Vanderbilt highlighted that the highly ionic bonds and the underlying wurtzite crystal structure of AlN, GaN, and InN systems lead to an electric polarization response that is one order of magnitude larger than in other more conventional III-V material systems such as zinc-blende GaAs [1]. On the one hand, compared to zinc-blende GaAs or InAs, the strain-induced piezoelectric response in wurtzite III-N materials is much larger. This originates in part from the fact that the wurtzite piezoelectric tensor has more nonvanishing and nonidentical components than the zinc-blende one [1]. Moreover, due to the underlying wurtzite crystal structure, III-N materials exhibit a so-called spontaneous polarization component, which is not present in zinc-blende III-V materials [1]. In addition to their interesting fundamental properties, wurtzite III-N materials and their respective alloys InGaN, AlGaN, and AlInN have attracted considerable interest for applications in high-power electronic and optoelectronic devices [17]. However, with the advent of nitride-based heterostructures grown along the polar wurtzite c axis, these built-in polarization vector fields present a major drawback for optoelectronic device applications such as light-emitting diodes (LEDs) or laser diodes (LDs), since they dominate their electronic and optical properties [18–22]. Here, fields of the order of MV/cm have been reported, leading for instance to extremely long radiative lifetimes (nanosecond regime) [23–25]. The long radiative lifetimes facilitate also nonradiative recombination processes, which are detrimental for efficient nitride-based LEDs [26]. But, it should be noted that the intrinsic polarization fields are beneficial for other nitride-based applications such as tunneling diodes and transistors [27,28].

Driven by the negative effect of these built-in fields for LEDs and LDs utilizing wurtzite III-N-based heterostructures, strategies to circumvent these fields have been targeted extensively [22,29–36]. These strategies range from polarization matching techniques [31,32] to the growth of so-called non- and semipolar nanostructures [30]. The underlying idea of non- and semipolar systems is that the growth axis is at a nonvanishing angle with the polar c axis of the wurtzite crystal [30]. With this technique III-N heterostructures, both quantum wells (QWs) and quantum dots (QDs), have been realized which exhibit reduced built-in fields [18,30,35]. However, when designing emitters utilizing non-c-plane systems or polarization matching techniques for c-plane systems, an accurate and detailed knowledge of the built-in electric field is required and even more importantly how these fields change with growth plane. Most studies of these polarization fields rely on descriptions similar to those introduced by Bernardini *et al.* [1], thus considering the piezoelectric response to be linear in strain.

For several years, a similar first-order approach has been used to describe piezoelectric fields in zinc-blende heterostructures such as InAs/GaAs QDs [4,37]. But, in recent years, several groups have reported that in addition to first-order piezoelectric contributions, second-order effects, quadratic in strain, play an important role in an accurate description of the piezoelectric vector fields and thus connected electronic and optical properties of these systems [6,9]. These second-order piezoelectric effects have been widely neglected in wurtzite III-N materials. Only recently second-order piezoelectric coefficients for GaN, AlN, and InN have been reported [11,12,38]. Based on these coefficients, electric fields in c-plane nitride-based QWs have been studied, showing that when including second-order piezoelectricity, in general, a better agreement between theory and experiment is achieved [11,38,39]. Furthermore, recent calculations on c-plane InGaN/GaN QDs with high In contents ($\geqslant$30%) gave clear indications that second-order piezoelectric effects are significant in these systems and have to be considered for an accurate description of the electronic and optical properties of these emitters [40]. While a limited number of calculations on c-plane systems is now available, there exist no detailed analysis of how second-order piezoelectricity affects the built-in field in semipolar QWs and/or semi- and nonpolar QDs. Given that first-order piezoelectric effects are strongly reduced in these systems, it is still an open question how important second-order contributions are for the total built-in field. This question is significant not only from a fundamental physics perspective; it is also essential from an application point of view, given the interest in these semi- and nonpolar nitride-based heterostructures for optoelectronic devices. In this study we address the question of the importance of second-order piezoelectricity for an accurate description of the electrostatic built-in fields in non-c-plane nitride-based QWs and QDs. We tackle this question here by means of a continuum-based framework. Thus in a first step we provide analytic expressions for first- and second-order piezoelectric polarization vector fields in semiconductors with a wurtzite crystal structure as a function of the incline angle θ to the c axis. The benefit of such a symmetry-adapted approach is twofold. First, this ansatz can be applied to any wurtzite system, e.g., III-N or ZnO. Second, the derived angle-dependent expressions can be included in existing QW or QD codes to calculate built-in fields and electronic and optical properties of these systems. Here we apply these expressions to III-N heterostructures. We find that second-order piezoelectric effects significantly affect the built-in potential and thus the electric field of semipolar growth planes with high incline angle values ($55^\circ \leqslant \theta \leqslant 85^\circ$ and $105^\circ \leqslant \theta \leqslant 120^\circ$). For instance, in a multi-QW (MQW) InGaN/GaN system with 22% In grown on the $(11\bar{2}2)$ plane the built-in electric field of this structure is increased by approximately 20% due to second-order piezoelectricity. Furthermore, by including second-order piezoelectric effects in the calculations, an improved agreement between calculated and experimentally reported electric field values in GaN/AlN and InGaN QWs is observed. Additionally, our calculations reveal that for GaN/AlN QD systems, second-order piezoelectric contributions are of secondary importance, at least for the here studied QD geometries and growth planes. This situation changes for $In_{0.2}Ga_{0.8}N$/GaN QDs grown on the semipolar $(11\bar{2}2)$ plane and for nonpolar a-plane systems. For example, in the nonpolar case, inside the dot, built-in potential contributions arising from first- and second-order piezoelectric contributions are comparable in magnitude but opposite in sign. This leads not only to a further reduction of the built-in potential but also to built-in potential profile changes. Overall, our calculations reveal that especially for InGaN/GaN-based semi- and nonpolar heterostructures, second-order piezoelectric contributions can have a significant impact on the electrostatic built-in fields in these structures.

The paper is organized as follows. Section II gives a general overview of the theoretical framework used here. We start in Sec. II A with a brief overview of electric polarization effects in wurtzite semiconductors. This is followed by a summary of the theoretical framework used here to study built-in fields in semiconductor nanostructures. In Sec. III we present the results of our studies. We start, in Sec. III A, with wurtzite III-N QW systems before turning to QD structures in Sec. III B. In Sec. III B 1 we focus on GaN/AlN QDs grown on different substrate orientations, while Sec. III B 2 is dedicated to InGaN/GaN QD systems, again grown along different crystallographic directions.

II. THEORY

To study the interplay of second-order piezoelectricity and growth plane on the total built-in field in wurtzite III-N systems, we present here our theoretical framework to perform such an analysis. In Sec. II A we start with a general overview of electric polarization effects in semiconductors. We then introduce briefly first- and second-order piezoelectric polarization vector fields for c-plane wurtzite systems as well as the spontaneous polarization. The general procedure to derive analytic expressions for the polarization vector fields for arbitrary growth planes will also be given. Analytic results for planes characterized by a single incline angle θ to the wurtzite c axis are presented in the Appendix. In Sec. II B we give a brief overview of the calculation framework applied.

A. Polarization vector fields in wurtzite III-N semiconductor nanostructures

Semiconductor materials with a lack of inversion symmetry exhibit an electric polarization under applied stress [1,4,6,8]. This strain-mediated electric polarization is the so-called piezoelectric polarization. In general this quantity can be expressed as follows [6]:

$$P_{\mathrm{pz},\mu} = \sum_{j=1}^{6} e_{\mu j}\epsilon_j + \frac{1}{2}\sum_{j,k=1}^{6} B_{\mu jk}\epsilon_j\epsilon_k + \cdots . \qquad (1)$$

To first order, the magnitude of piezoelectric response is connected to strain ϵ_j (Voigt notation) via the first-order piezoelectric tensor $e_{\mu j}$. This first-order ansatz is linear in strain. In general, higher-order effects, e.g., components quadratic in strain, can also be described in this approach. In the following we focus our attention on second-order piezoelectric effects arising thus from the components $B_{\mu jk}$; cf. Eq. (1). In general, it should be stressed that the second-order piezoelectric effect is not just a second-order term in a polynomial expansion of the piezoelectric response of a material. Pal *et al.* [11] have already

pointed this out for III-N materials. Additionally, Beya-Wakata *et al.* [10] and Caro *et al.* [15] highlighted in their work on zinc-blende III-V materials that in certain materials second-order effects can dominate over first-order contributions, even for small strain. Fundamentally different factors contribute to first- and second-order piezoelectricity, for example, linear and nonlinear contributions to internal strain parameters and the material electronic response [15]. Furthermore, the symmetry of the underlying crystal structure of the material under consideration determines the number of nonvanishing and independent piezoelectric coefficients $e_{\mu j}$ and $B_{\mu jk}$ [8].

For systems with a wurtzite crystal structure one is left with 18 first-order coefficients $e_{\mu j}$ of which only three are independent quantities, namely e_{33}, e_{15}, and e_{31} [41,42]. Taking this into account and considering only first-order contributions in Eq. (1) one is left with the widely used and well-known c-plane piezoelectric polarization vector field $\mathbf{P}_{\mathrm{pz}}^{\mathrm{FO}}$ [42]:

$$\mathbf{P}_{\mathrm{pz}}^{\mathrm{FO}} = \begin{pmatrix} 2e_{15}\epsilon_{xz} \\ 2e_{15}\epsilon_{yz} \\ e_{31}(\epsilon_{xx}+\epsilon_{yy})+e_{33}\epsilon_{zz} \end{pmatrix}. \tag{2}$$

Please note, in Eq. (2) we have used the Cartesian notation for the strain tensor ϵ_{ij}; in Eq. (1) Voigt notation ϵ_j has been applied. The connection between these notations is given by $\epsilon_1 = \epsilon_{xx}, \epsilon_2 = \epsilon_{yy}, \epsilon_3 = \epsilon_{zz}, \epsilon_4 = (\epsilon_{yz}+\epsilon_{zy}) = 2\epsilon_{yz}$, $\epsilon_5 = (\epsilon_{xz}+\epsilon_{zx}) = 2\epsilon_{xz}$, $\epsilon_6 = (\epsilon_{xy}+\epsilon_{yx}) = 2\epsilon_{xy}$ [41]. More details on the connection between Voigt and Cartesian notation can be found in Ref. [41]. From Eq. (2) it is clear that x and y components are determined by shear strain ϵ_{ij} (Cartesian notation), with $i \neq j$, and the first-order piezoelectric coefficient e_{15}. The z component is determined by the diagonal parts of the strain tensor ϵ_{ii} and the two piezoelectric coefficients e_{31} and e_{33}.

Having introduced first-order piezoelectric contributions, we now turn and focus on second-order piezoelectric contributions related to $B_{\mu jk}$. Based on symmetry considerations, for instance given by Grimmer [8], one can show that $B_{\mu jk}$ has 17 nonvanishing components of which 8 are independent. Using this information and Eq. (1), for a c-plane system where the z axis of the coordinate system is parallel to the wurtzite c axis, the second-order piezoelectric polarization vector field $\mathbf{P}_{\mathrm{pz}}^{\mathrm{SO}}$ is given by

$$\mathbf{P}_{\mathrm{pz}}^{\mathrm{SO}} = \begin{pmatrix} 2B_{115}(\epsilon_{xx}\epsilon_{xz}+\epsilon_{xy}\epsilon_{yz})+2B_{135}\epsilon_{zz}\epsilon_{xz}-2B_{125}(\epsilon_{xy}\epsilon_{yz}-\epsilon_{yy}\epsilon_{xz}) \\ 2B_{115}(\epsilon_{yy}\epsilon_{yz}+\epsilon_{xy}\epsilon_{xz})+2B_{135}\epsilon_{zz}\epsilon_{yz}+2B_{125}(\epsilon_{xx}\epsilon_{yz}-\epsilon_{xy}\epsilon_{xz}) \\ \frac{B_{311}}{2}\left(\epsilon_{xx}^2+\epsilon_{yy}^2+2\epsilon_{xy}^2\right)+B_{312}\left(\epsilon_{xx}\epsilon_{yy}-\epsilon_{xy}^2\right)+B_{313}(\epsilon_{xx}\epsilon_{zz}+\epsilon_{yy}\epsilon_{zz})+2B_{344}\left(\epsilon_{yz}^2+\epsilon_{xz}^2\right)+\frac{1}{2}B_{333}\epsilon_{zz}^2 \end{pmatrix}. \tag{3}$$

Again, Cartesian strain notation has been used here. In comparison to the first-order piezoelectric polarization vector field, cf. Eq. (2), the interplay of the different strain contributions is far more complicated. The x and y components no longer just depend on shear strain components ϵ_{ij} $(i \neq j)$. Here also products of shear strain parts and diagonal components ϵ_{ii} arise. Furthermore, the z component is now not only dependent on diagonal parts of the strain tensor ϵ_{ii}; also shear strain components become important. Moreover, the increased number of second-order piezoelectric coefficients $B_{\mu jk}$, especially related to shear strains, presents also a significant difference compared to the first-order piezoelectric component. This means that one could expect that in systems where shear strain contributions are significant, e.g., semipolar wurtzite QWs, second-order piezoelectricity is important for an accurate description of the connected electrostatic built-in fields.

In addition to the strain-induced piezoelectric polarization, the wurtzite crystal structure also gives rise to a so-called spontaneous polarization, which is present even in the absence of strain [1,42]. This quantity originates from the lack of inversion symmetry of the wurtzite crystal along the c axis and is a constant vector field along this direction. Thus in a standard c-plane description, where the c axis is usually parallel to the z axis of the coordinate system, the spontaneous polarization vector field $\mathbf{P}_{\mathrm{SP}}$ reads [42]

$$\mathbf{P}_{\mathrm{SP}} = \begin{pmatrix} 0 \\ 0 \\ P_{\mathrm{sp}} \end{pmatrix}. \tag{4}$$

Overall, the total polarization vector field $\mathbf{P}_{\mathrm{Tot}}$ in a wurtzite system is the sum of piezoelectric and spontaneous polarization vector fields, $\mathbf{P}_{\mathrm{Tot}} = \mathbf{P}_{\mathrm{SP}} + \mathbf{P}_{\mathrm{pz}}^{\mathrm{FO}} + \mathbf{P}_{\mathrm{pz}}^{\mathrm{SO}}$.

In general, in wurtzite III-N-based heterostructures the polarization vector field of the barrier material is different from the polarization vector field in the active region. This originates from the fact that for instance the strain state of the active region is different from that of the barrier material [32]. Consequently, this gives rise to a charge density ρ_p, which can be described by [9,43,44]

$$\rho_p = -\nabla \cdot \mathbf{P}_{\mathrm{Tot}}, \tag{5}$$

where $\mathbf{P}_{\mathrm{Tot}}$ is the total polarization vector field. In the absence of external charges, the connected electrostatic built-in potential ϕ_p can be calculated from [9,44]

$$\nabla \cdot \mathbf{D} = 0, \tag{6}$$

where the displacement field $\mathbf{D}$ is given by

$$\mathbf{D} = \epsilon_0 \epsilon_r(\mathbf{r}) \nabla \phi_p + \mathbf{P}_{\mathrm{Tot}}. \tag{7}$$

Thus, the electrostatic built-in potential ϕ_p can be obtained by solving Poisson's equation [9,43,44]:

$$\nabla \cdot [\epsilon_0 \epsilon_r(\mathbf{r}) \nabla \phi_p] = -\nabla \cdot \mathbf{P}_{\mathrm{Tot}} = \rho_p. \tag{8}$$

This scheme is a widely used approach in the literature to calculate electrostatic built-in potentials in semiconductor heterostructures [9,27,36,45].

In order to study the electrostatic built-in potential ϕ_p of wurtzite III-N heterostructures, such as QWs and more

challenging QDs, grown on different crystallographic planes one has different options to address this question. One option is to directly use the c-plane expressions for $\mathbf{P}_{\mathrm{pz}}^{\mathrm{FO}}$ [Eq. (2)], $\mathbf{P}_{\mathrm{pz}}^{\mathrm{SO}}$ [Eq. (3)], and $\mathbf{P}_{\mathrm{SP}}$ [Eq. (4)] and rotate the nanostructure under consideration inside a c-plane-based simulation box. In this case the z axis of the supercell is always parallel to the wurtzite c axis. While this approach is in principle straightforward to implement, it may suffer from discretization problems inside the simulation cell, given that a variety of different non-c-plane systems are of topical interest and complicated QD geometries have been reported [46–50]. For example, the semipolar $(11\bar{2}2)$ plane, which is described by an incline angle θ of 58°, is of relevance for growth of both QWs and QDs [47,49]. QD geometries reported for this plane are rectangle-based truncated pyramids or arrowhead-like in shape, and exhibit different incline angles for the different side facets [49]. All this might lead to the situation that very fine mesh sizes are required to avoid numerical artifacts arising from such an approach in which the dot geometry inside the simulation cell is rotated. Thus, calculations might be numerically heavy. The second option to study the built-in potential of non-c-plane-based systems is to rotate the expressions for the polarization vector fields and strain tensors directly instead of rotating the nanostructure geometry. In this case the z axis of the simulation cell is always along the growth direction of the nanostructure. This might now allow us more easily to use different discretization step sizes along different directions, reducing therefore the computational effort of the method. For this ansatz analytic expressions for the different quantities are required, for instance as a function of the incline angle θ to the wurtzite c axis. In nitride-based *QWs* and for first-order piezoelectricity this is a widely used approach [29,46,47,51]. However, all these works do not account for second-order piezoelectric effects. But, once the analytic expression for $\mathbf{P}_{\mathrm{pz}}^{\mathrm{SO}}$ as a function of θ is known, it can be easily implemented in existing symmetry-adapted QW codes. We provide this expression for $\mathbf{P}_{\mathrm{pz}}^{\mathrm{SO}}$, along with the one for $\mathbf{P}_{\mathrm{pz}}^{\mathrm{FO}}$, in the Appendix. When treating the QW as a one-dimensional system, only the z component of the total polarization vector field is required for calculating the built-in potential. For QD systems, due to their three-dimensional confinement, the x, y, and z components are relevant. Thus the expressions provided here allow for the calculation of electrostatic built-in potentials of both QD and QW systems grown along arbitrary crystallographic directions characterized by the incline angle θ.

As discussed already above, the explicit expressions for $\mathbf{P}_{\mathrm{pz}}^{\mathrm{FO}}$, $\mathbf{P}_{\mathrm{pz}}^{\mathrm{SO}}$, and $\mathbf{P}_{\mathrm{SP}}$ are given in the Appendix; here we summarize briefly the strategy to obtain these expressions and how to generalize the approach further. Similarly to Refs. [29] and [45] we transform the conventional coordinate system (x,y,z), in which the wurtzite c axis is parallel to the z axis, to a primed coordinate system (x',y',z'), using a matrix U that describes a rotation around the y axis [52]:

$$U = \begin{pmatrix} \cos\theta & 0 & -\sin\theta \\ 0 & 1 & 0 \\ \sin\theta & 0 & \cos\theta \end{pmatrix}. \tag{9}$$

Here θ denotes the angle measured with respect to the c axis. This approach can be generalized by considering a second rotation described by the angle φ around the z axis. In this more general case, relevant for instance in nanowire systems [53] or basal plane stacking faults where the wurtzite and zinc-blende phase (oriented along the [111] direction) are mixed [54], a rotation matrix $\tilde{U}$ reads [52]

$$\tilde{U} = \begin{pmatrix} \cos\theta\cos\varphi & \cos\theta\sin\varphi & -\sin\theta \\ -\sin\varphi & \cos\varphi & 0 \\ \sin\theta\cos\varphi & \sin\theta\sin\varphi & \cos\theta \end{pmatrix}. \tag{10}$$

For $\varphi = 0$, $\tilde{U}$ reduces to U defined in Eq. (9). Further generalization can be achieved by considering a third angle (Euler angles). Rotation matrices for that case are given for example in Ref. [55]. Assuming a general rotation matrix U^{gen}, vectors $\mathbf{k}$ and tensors ϵ are transformed to the primed coordinate system via [52,55]

$$k_i' = \sum_{\alpha} U_{i\alpha}^{\mathrm{gen}} k_\alpha, \quad \epsilon_{ij}' = \sum_{\alpha,\beta} U_{i\alpha}^{\mathrm{gen}} U_{j\beta}^{\mathrm{gen}} \epsilon_{\alpha\beta}. \tag{11}$$

As discussed above, for all our studies here we are using $U^{\mathrm{gen}} = U$ defined in Eq. (9), which describes a rotation around the y axis.

So far we have introduced general aspects of the polarization vector fields and connected electrostatic potentials in wurtzite semiconductor heterostructures up to second-order piezoelectricity. In the next step we briefly discuss the theoretical framework in which our calculations have been carried out. We will also briefly review the material parameters used in the present study.

B. Theoretical framework

Equipped with the analytic expressions for spontaneous and first- and second-order piezoelectric polarization vector fields as a function of θ, cf. the Appendix, these terms have been implemented in the highly flexible plane-wave-based software library S/Phi/nX [60,61]. In general, S/Phi/nX allows for defining arbitrary elastic and piezoelectric tensors as well as $\mathbf{k}\cdot\mathbf{p}$ Hamiltonians. All ingredients of the modeling process, including the nanostructure's geometry and required material input parameters, are defined in human-readable input files. Within this framework, once all the analytic expressions are known, no further coding is required.

In the following we study the impact of second-order piezoelectric effects on the electrostatic built-in fields in nitride-based QW and QD structures grown along different crystallographic directions. In Eqs. (5)–(8) we have already outlined the main ingredients and how to calculate the electrostatic built-in potential ϕ_p once the polarization vector field is known. However, as further input the (position-dependent) strain tensor ϵ_{ij} of the system under consideration is required. Here, we use a continuum-based approach to calculate the strain tensor components. Using continuum-elasticity theory, the total elastic energy F of the simulation box is minimized with respect to the displacement field $\mathbf{u}(\mathbf{r})$ [60,62]. F can be written as [62]

$$F = \frac{V}{2} \sum_{ijkl} C_{ijkl}\epsilon_{ij}\epsilon_{kl}, \tag{12}$$

TABLE I. Material parameters for GaN, InN, and AlN used in this study. Elastic constants are denoted by C_{ij}, first-order piezoelectric coefficients by $e_{\mu j}$, and second-order ones by $B_{\mu jk}$. The spontaneous polarization is given by $P_{\rm sp}$ and related bowing parameters for InGaN and AlGaN are denoted as $b_{\rm sp}$. The dielectric constant is given by ϵ_r.

Parameter	GaN	InN	AlN
$a_{\rm lat}$ (Å) [56]	3.189	3.545	3.112
$c_{\rm lat}$ (Å) [56]	5.185	5.703	4.982
C_{11} (GPa) [57]	368.6	233.8	410.2
C_{12} (GPa) [57]	131.6	110.0	142.4
C_{13} (GPa) [57]	95.7	91.6	110.1
C_{33} (GPa) [57]	406.2	238.3	385.0
C_{44} (GPa) [57]	101.7	55.4	122.9
e_{15} (C/m^2) [58]	−0.32	−0.42	−0.39
e_{31} (C/m^2) [58]	−0.44	−0.58	−0.63
e_{33} (C/m^2) [58]	0.74	1.07	1.46
B_{115} (C/m^2) [38]	3.8	4.5	4.4
B_{125} (C/m^2) [38]	2.3	2.8	2.4
B_{135} (C/m^2) [38]	2.7	1.6	−0.1
B_{311} (C/m^2) [38]	6.2	4.8	3.0
B_{312} (C/m^2) [38]	3.3	3.7	3.0
B_{313} (C/m^2) [38]	0.4	0.5	3.8
B_{333} (C/m^2) [38]	−21.4	−18.6	−26.0
B_{344} (C/m^2) [38]	0.4	0.5	3.2
$P_{\rm sp}$ (C/m^2) [58]	−0.040	−0.049	−0.091
ε_r [45]	9.6	15.3	8.5
		InGaN	
$b_{\rm sp}$ (C/m^2) [59]		−0.037	
			AlGaN
$b_{\rm sp}$ (C/m^2) [59]			−0.0191

where V denotes the volume of the system and C_{ijkl} are the elastic constants of the materials in question. The strain tensor components, given in Cartesian notation, are denoted by ϵ_{ij} and ϵ_{kl}. As detailed in Refs. [29] and [45], to obtain the strain field of a wurtzite nitride-based nanostructure in our rotated theoretical framework, also the stiffness tensor C_{ijkl} needs to be known as a function of the incline angle θ to the c axis. The analytic expressions for $C_{ijkl}(\theta)$ are given, for example, in Ref. [45].

In addition to the QW dimensions and QD geometries, which will be discussed below, material parameters are required as input. In the following we focus our attention on systems based on InN, GaN, AlN and their respective alloys. Table I summarizes the here used material parameters for the binary materials. It should be noted that compared to other material systems, such as InAs or GaAs, there is still a large degree of uncertainty in many of the nitride-material parameters [32,56,63–65]. For example, even though several groups have measured and calculated first-order piezoelectric coefficients, the values might scatter significantly and even different signs for the shear-strain-related piezoelectric coefficient e_{15} have been reported [66,67]. However, all recent studies point towards a negative sign of e_{15} [10–12,39,52], and thus we have chosen a data set with $e_{15} < 0$ [58].

While there are several reports on first-order piezoelectric coefficients, only very few studies have been performed to extract second-order piezoelectric coefficients $B_{\mu jk}$ for wurtzite III-N systems [11,12,38]. In the following we use the parameter set by Prodhomme *et al.* [38] since it contains for the material systems InN, GaN, and AlN values for all nonvanishing coefficients $B_{\mu jk}$. Thus it provides a consistent parameter set for our study here.

Overall, our main focus is to gain insight into trends of how second-order piezoelectric effects affect the electrostatic built-in fields of nitride-based nanostructures grown on different substrate orientations. Therefore, to describe alloys we assume a linear interpolation for all material parameters except the spontaneous polarization, where we apply the bowing parameters $b_{\rm SP}$ from Ref. [59]. Further, more detailed calculations, looking at the impact and importance of different material parameter sets and the choice of bowing parameters, can be performed in a straightforward way once these quantities are known. However, this is beyond the scope of the present study where we are interested in general effects.

III. RESULTS

Having established the theoretical framework in the previous section, we analyze now how second-order piezoelectric effects impact the built-in field of nitride-based QWs and QDs grown along different crystallographic directions. In a first step, in Sec. III A, we focus on QW structures and study polarization fields for different material combinations and growth directions. In Sec. III B we turn our attention to the built-in potential in QD structures grown on different substrate orientations.

A. Built-in fields in wurtzite III-N QWs grown along different crystallographic directions

An ideal QW structure can be treated as a one-dimensional system since quantum confinement is present along one direction only. We use this approximation here and start from c-plane structures where the c axis is parallel to the z axis of the coordinate system. Based on our theoretical framework introduced above, in the following the QW growth direction is always the z' axis of the rotated coordinate system. In this one-dimensional problem discontinuities in the polarization vector field $\mathbf{P}$ occur only along the growth direction. Therefore, only the z' component of $\mathbf{P}$ is relevant for a QW structure. The situation is more complex for a QD system where the three-dimensional confinement of the dot comes into play and the full polarization vector field needs to be considered. This question will be addressed in Secs. III B 1 and III B 2. Here, to gain insight into the interplay of second-order piezoelectricity and growth plane, we start with the most extreme cases by studying GaN/AlN, InN/AlN, and InN/GaN systems. Figure 1 displays the z' component of the different contributions to the full *piezoelectric* response, $P^{\rm FO}_{{\rm PZ},z'} + P^{\rm SO}_{{\rm PZ},z'}$, as a function the incline angle θ for GaN/AlN [Fig. 1(a)], InN/AlN [Fig. 1(b)], and InN/GaN [Fig. 1(c)]. To shed light onto the importance of the second-order piezoelectric contribution, results are shown for (i) "standard" first-order terms only, $P^{\rm FO}_{{\rm pz},z'}$ (red circles), (ii) taking only second-order piezoelectric effects into account, $P^{\rm SO}_{{\rm pz},z'}$ (black squares), and (iii) the sum of first- and second-order components $P^{\rm FO}_{{\rm pz},z'} + P^{\rm SO}_{{\rm pz},z'}$ (blue triangles). The vertical dashed lines in Fig. 1 indicate some of the

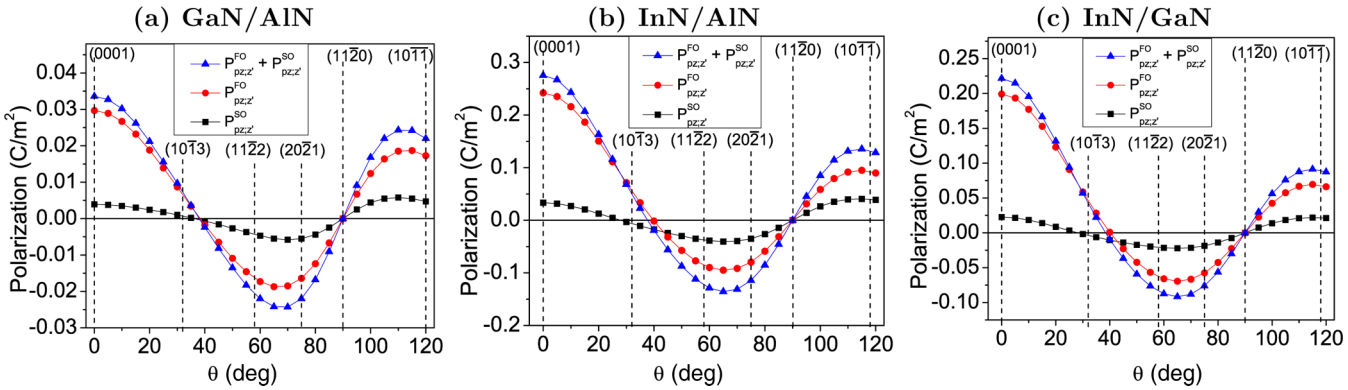

FIG. 1. z' component of piezoelectric polarization vector fields in (a) GaN/AlN, (b) InN/AlN, and (c) InN/GaN systems as a function of the incline angle θ to the wurtzite c axis. The contributions arising from first-order piezoelectricity are denoted by (red) circles. Contributions entirely stemming from second-order piezoelectricity are given by (black) squares. The total piezoelectric polarization, which includes first- and second-order piezoelectric polarization, is given by (blue) triangles. Dashed vertical lines indicate selected experimentally relevant growth planes.

experimentally relevant growth planes for semi- and nonpolar nitride-based QWs [46,71–74]. Overall, for the three systems under consideration, the second-order contribution (black squares) is smaller than the first-order contribution (red circles). Furthermore, we find that for certain planes, for instance the (10$\bar{1}$3) plane, second-order piezoelectricity has a negligible effect on the z' component of the total piezoelectric polarization vector field. This originates from the fact that the second-order contribution is changing sign around this angle ($\theta \approx 30^\circ$). However, for c-plane systems and structures grown on planes described by θ values in the range of $55^\circ \leqslant \theta \leqslant 80^\circ$ and $105^\circ \leqslant \theta \leqslant 120^\circ$, the magnitude of the total piezoelectric polarization (blue triangles) is clearly increased by second-order piezoelectricity. More specifically, for the polar c-plane structures ($\theta = 0^\circ$) of the three different systems studied here, the full piezoelectric polarization values increase by 11%–14% when taking second-order piezoelectric effects into account. It should be noted that this increase is consistent with the c-plane results presented in Ref. [11] where a different first- and second-order piezoelectric coefficient set has been used. However, the c-plane data presented in Ref. [38], applying a slightly different first-order parameter set $e_{\mu j}$ but the same second-order parameter set $B_{\mu jk}$, indicated a decrease in $P^{\mathrm{FO}}_{\mathrm{pz},z'} + P^{\mathrm{SO}}_{\mathrm{pz},z'}$ for InN/GaN systems when compared to $P^{\mathrm{FO}}_{\mathrm{pz},z'}$ only. Based on a closer inspection of the results in Ref. [38] we relate the observed reduction in $P^{\mathrm{FO}}_{\mathrm{pz},z'} + P^{\mathrm{SO}}_{\mathrm{pz},z'}$ to differences in the applied Poisson ratio/biaxial coefficient. In our case we assume for all the systems studied here a homogenous biaxial strain along the z' axis. For a c-plane system this results in $\epsilon_{zz} = -\frac{2C_{13}}{C_{33}}\epsilon_{xx}$. As input we use the parameters given in Table I.

Turning to the semipolar planes, where the magnitude of $P^{\mathrm{FO}}_{\mathrm{pz},z'}$ is reduced compared to the c-plane system, the impact of the second-order piezoelectric effect is even larger. For example, at $\theta = 75^\circ$, the (20$\bar{2}$1) plane, the magnitude of the overall piezoelectric response changes by 33%, 44%, and 32% for GaN/AlN, InN/AlN, and InN/GaN systems, respectively, when second-order piezoelectric effects are included.

Based on these general trends we discuss now how second-order piezoelectric effects affect the built-in electric field in nitride-based QWs grown on different substrate orientations. For this analysis we focus on two material systems, namely GaN/AlN- and InGaN/GaN-based QWs. Such structures have been studied experimentally in the literature for different substrate orientations [72–76]. To be able to compare our theoretical results to experimental literature data, we calculate the built-in field inside a multi-QW (MQW) system via [11]

$$F_p(\theta) = -\frac{\left[P^B_{\mathrm{sp},z'}(\theta) - P^W_{\mathrm{sp},z'}(\theta)\right] + \left[P^B_{\mathrm{pz},z'}(\theta) - P^W_{\mathrm{pz},z'}(\theta)\right]}{\epsilon^W_r + \epsilon^B_r(t^W/t^B)}. \tag{13}$$

Here t^W (t^B) is the QW (barrier) thickness and $P^W_{\mathrm{sp},z'}(\theta)$ [$P^B_{\mathrm{sp},z'}(\theta)$] is the angle-dependent spontaneous polarization in the well (barrier). The angle-dependent piezoelectric polarization in the well (barrier) is denoted by $P^W_{\mathrm{pz},z'}(\theta)$ [$P^B_{\mathrm{pz},z'}(\theta)$].

Equipped with Eq. (13) and the analytic expressions given in the Appendix, we can now compare calculated and measured built-in electric fields. The results are summarized in Table II. It should be noted that only a few experimental reports on built-in fields in QW structures grown on semipolar planes are available in the literature [72]. To highlight the impact of the second-order piezoelectric polarization, calculations using Eq. (13) have been performed in the absence and in the presence of second-order contributions. In the absence of second-order piezoelectricity, $P^W_{\mathrm{pz},z'} = P^{\mathrm{FO}}_{\mathrm{pz},z'}$, only first-order piezoelectric coefficients $e_{\mu j}$ are relevant. In the presence of first- and second-order effects, $P^W_{\mathrm{pz},z'} = P^{\mathrm{FO}}_{\mathrm{pz},z'} + P^{\mathrm{SO}}_{\mathrm{pz},z'}$, $P^W_{\mathrm{pz},z'}$ is determined by the combined contributions of both $e_{\mu j}$ and $B_{\mu jk}$. Overall, as expected from our discussion above, when including second-order effects in the calculations, the magnitude of the electric field is increased when compared to a standard first-order-only calculation for both GaN/AlN and InGaN/GaN systems; cf. Table II. One can also conclude from Table II that the second-order piezoelectric contributions have a larger impact on the magnitude of the built-in field in semipolar structures and changes of 12%–14% in magnitude are observed. In general, when comparing the calculated fields to the experimental data, we find that with first-order piezoelectricity only the theoretical values underestimate the

TABLE II. Built-in electric fields in GaN/AlN and InGaN/GaN multiple quantum well structures. The well (barrier) thickness is denoted by t^W (t^B). The growth plane, and thus the incline angle to the c axis, is given by θ. Experimental data taken from the literature are denoted by $F_{\mathrm{p,exp}}$. Our theoretical data including only first-order piezoelectricity and spontaneous polarization are given by $F_{\mathrm{p,theo}}^{\mathrm{FO+SP}}$. The results of the full calculation, including second-order piezoelectric effects, are denoted by $F_{\mathrm{p,theo}}^{\mathrm{FO+SO+SP}}$.

Material	t^W (nm)	t^B (nm)	θ (deg)	$F_{\mathrm{p,exp}}$ (kV/cm)	$F_{\mathrm{p,theo}}^{\mathrm{FO+SP}}$ (kV/cm)	$F_{\mathrm{p,theo}}^{\mathrm{FO+SO+SP}}$ (kV/cm)
GaN/AlN	2.6	100	0	1020 [68]	957	1004
GaN/AlN	2.5	6	0	800 [69]	710	744
GaN/AlN	2.3	1.9	0	504 [70]	465	488
GaN/AlN	1.4	1.9	0	607 [70]	586	614
$In_{0.12}Ga_{0.88}N$/GaN	3	6	0	1600 [71]	1530	1620
$In_{0.12}Ga_{0.88}N$/GaN	4	30	58	-575 ± 150 [72]	-397	-444
$In_{0.15}Ga_{0.85}N$/GaN	4	30	118	840 ± 150 [72]	587	666
$In_{0.06}Ga_{0.94}N$/GaN	3	3	0	610 [71]	593	610
$In_{0.22}Ga_{0.78}N$/GaN	3	8	0	3090 [71]	2940	3220
$In_{0.09}Ga_{0.91}N$/GaN	3	3	0	1000 [71]	880	920

magnitude of the electric field in the respective structures. When including second-order piezoelectricity, an improved agreement between theory and experiment is observed.

To study the impact of the second-order piezoelectric effect on the electric field in more detail and how the growth plane contributes to this, $F_p(\theta)$ is shown as a function of the incline angle θ for different $In_xGa_{1-x}N$/GaN QW systems in Fig. 2. The electric field $F_p(\theta)$, Eq. (13), has been calculated for three different In contents x, namely 12%, 15%, and 22%. For the 12% and 15% In system we use the experimental results in terms of well and barrier thickness given in Ref. [72] based on $(11\bar{2}2)$- and $(10\bar{1}1)$-oriented MQWs. Applying the experimental findings of Ref. [72], well and barrier thickness are chosen to be $t^W = 4$ nm and $t^B = 30$ nm [72], respectively. For the 22% In MQW system the settings reported by Hangleiter *et al.* [71] for a (0001)-oriented system have been used ($t^W = 3$ nm, $t^B = 8$ nm) [71]. When varying the incline angle θ in our calculations the barrier and QW thicknesses of the here considered structures have been kept constant to achieve a consistent comparison. Figure 2(a) displays the calculated electric field in the absence of second-order contributions to the piezoelectric polarization in $P^W_{\mathrm{pz},z'}$; cf. Eq. (13). Given the strain dependence of the piezoelectric polarization, the total electric field is largest in the sample with the highest In content (blue triangle). Independently of the In content, at $\theta \approx 45^\circ$ and $\theta = 90^\circ$ the electric field changes sign. When including second-order contributions in the calculations, cf. Fig. 2(b), this behavior of zero electric field and sign change is approximately unaffected. However, the magnitude of the electric field, independent of the incline angle θ, is always increased. To flesh out this effect even more clearly, Fig. 2(c) depicts the electric field increase in percent obtained from the difference between the results displayed in Figs. 2(a) (no second-order contributions) and 2(b) (with second-order effects). The data further confirm that especially for semipolar planes, where fields are significantly reduced compared to the c-plane structures, second-order effects can play an important role in an accurate description of the built-in fields in these structures. More specifically, for the $(20\bar{2}1)$ plane ($\theta = 75^\circ$) the magnitude of the electric field increases by 11%, 13%, 18% for an In content of 12%, 15%, and 22%, respectively, due to second-order piezoelectricity.

Having presented a detailed analysis of the impact of second-order piezoelectric effects on the electric built-in fields in nitride-based QWs grown along different crystallographic directions, we turn now to discuss nitride-based QDs. The results of this analysis are presented in the following section.

B. Built-in potential in wurtzite III-N QDs grown along different crystallographic directions

In this section we focus our attention on the impact of the second-order piezoelectric effect on the electrostatic built-in potential in nitride-based QDs. Again, special attention is paid to the impact of the growth plane on the results. To focus entirely on changes arising from second-order piezoelectric effects and the growth plane, we keep the QD geometry fixed throughout this study. A detailed analysis of the impact of the QD geometry is beyond the scope of the present analysis. Furthermore, given the three-dimensional QD geometry, the built-in potential and thus the electric field inside and around the nanostructure are position dependent. Thus, and in contrast to the QW systems discussed above, these quantities cannot be characterized by a single number. Therefore, instead of varying the incline angle θ continuously, we focus on selected experimentally relevant growth planes. In addition to c-plane InGaN/GaN and GaN/AlN QD systems, QD growth on the $(11\bar{2}2)$ plane has also been reported in the literature [48,73,74]. Also, both InGaN/GaN and GaN/AlN QDs have been grown on the nonpolar a plane [75–80]. In the following, we have directed our attention towards these three planes. For these studies we have assumed a lens-shaped geometry, which has also been considered in other theoretical works [81–83]. A QD base diameter of 14 nm and a height of 3 nm has been used in all calculations. These values are in the range of experimentally reported dimensions for dots grown on different planes [80,84]. Moreover, for the InGaN/GaN QD systems studied here, we consider an In content of 20%, in line with several experimental reports on c and nonpolar systems [75,76,85].

Starting from this information, the calculated built-in potentials for GaN/AlN QDs grown on different substrate orientations are discussed in Sec. III B 1. The results for the $In_{0.2}Ga_{0.8}N$/GaN QDs are presented in Sec. III B 2.

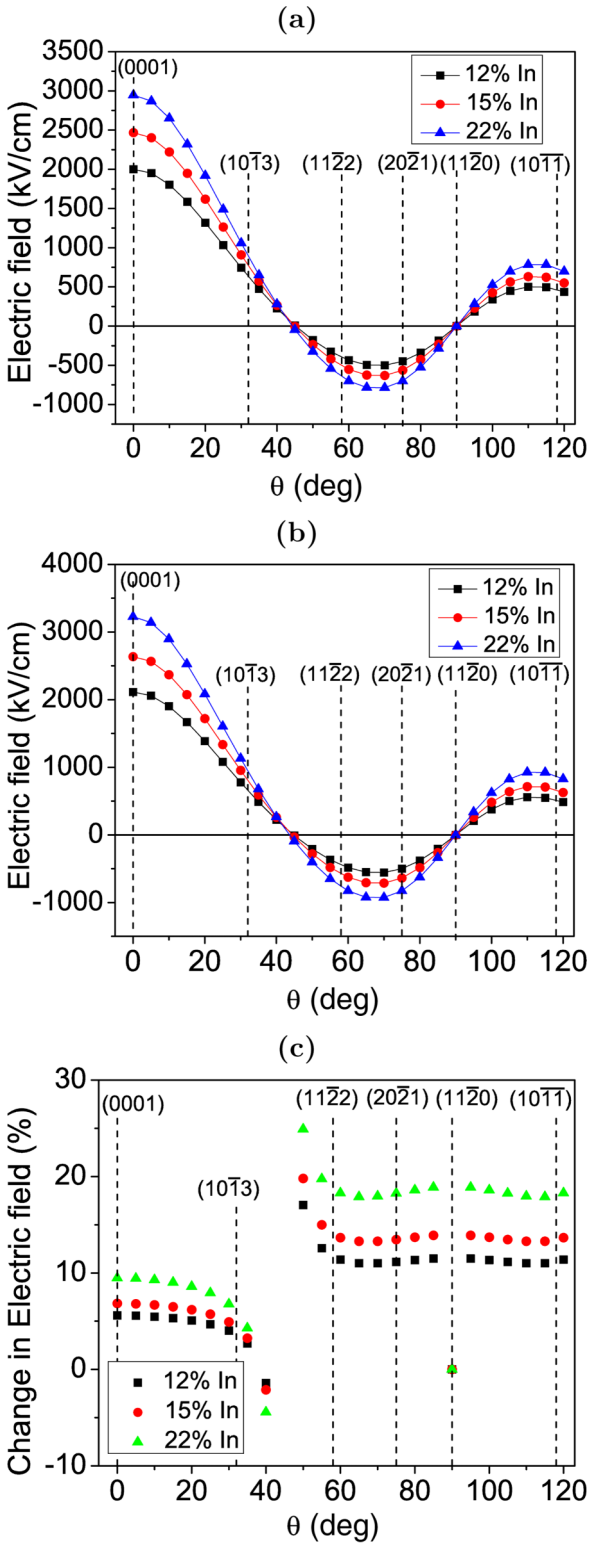

FIG. 2. Built-in electric field in InGaN/GaN multi-QWs (MQWs) as a function of the incline angle θ to the wurtzite c axis. Results for MQW systems with 12% In (black square), 15% In (red circle), and 22% (blue triangle) are displayed. More details about the systems are given in Table II and in the text. (a) Only first-order piezoelectricity and spontaneous polarization components are taken into account. (b) First- and second-order piezoelectricity as well as spontaneous polarization are included in the calculations. (c) Relative changes in the electric field due to second-order piezoelectric effects.

1. Built-in potentials in GaN/AlN QDs grown on different substrate orientations

Figure 3 shows contour plots of the electrostatic built-in potential ϕ_p in GaN/AlN QDs grown along different crystallographic directions. The first row displays the results for the c-plane case ($\theta = 0°$), the middle one for the semipolar ($11\bar{2}2$) system ($\theta = 58°$), and the lowest row depicts data for the nonpolar structure ($\theta = 90°$). Here a slice through the QD center in the x'-z' plane is chosen where the z' axis is always parallel to the growth direction. The (blue) dashed lines indicate the QD geometry. In the left column, Fig. 3(a), the results of the calculations in the absence of second-order piezoelectric contributions are depicted. Thus only "standard" first-order piezoelectric effects and the spontaneous polarization are taken into account. The middle column, Fig. 3(b), shows the second-order piezoelectric contribution on its own. This means that calculations in the absence of spontaneous and first-order piezoelectric polarization have been performed. The results of the full calculation, including first- and second-order piezoelectricity as well as the spontaneous polarization, are displayed in Fig. 3(c), right column. We start our analysis by looking at Fig. 3(a), thus neglecting second-order piezoelectricity. In the case of the c-plane system, the upper part of Fig. 3(a), we observe the well-known, very strong potential drop across the nanostructure along the growth direction. This particularity of the potential profile has the effect of spatially separating electron and hole wave functions along the growth direction and results in strongly increased radiative lifetimes when compared to situations without such a field [86]. Turning to the semipolar case, the middle part of Fig. 3(a), we find, as expected from our discussion above, a strongly reduced built-in potential. This stems from the fact that the c axis describes now a nonvanishing angle with the growth direction. Thus, the potential drop does not occur along the growth direction but still along the direction of the c axis. Finally, when turning to the nonpolar case, the lower part of Fig. 3(a), we find that the built-in potential is not zero as in the QW. This is attributed to the fact that the QD still exhibits facets oriented along the c axis [87,88]. Interestingly, for the dot geometry chosen here, the magnitude of the built-in potential in the nonpolar case is comparable to the magnitude of the built-in potential in the semipolar system. Thus, in terms of the built-in potential magnitude, our calculations do not indicate a significant improvement when moving from the ($11\bar{2}2$) system to the nonpolar growth plane. However, it should be noted that this feature could be related to the particular QD geometry chosen here. When considering different QD geometries, which could and probably will vary between the two growth planes, the situation might be different. We will come back to the question of the QD geometry further below.

We now turn to discussing second-order piezoelectric effects. To do so, we neglect spontaneous polarization and first-order piezoelectricity and focus on the second-order piezoelectric contribution only. The data of this investigation are shown in Fig. 3(b). Before looking into the results in detail, please note the different potential scales between Figs. 3(a) and 3(b). When comparing Figs. 3(a) and 3(b), we clearly observe that for GaN/AlN QDs second-order piezoelectric effects, at least for the chosen dot geometry, are significantly smaller when compared to the combined spontaneous and

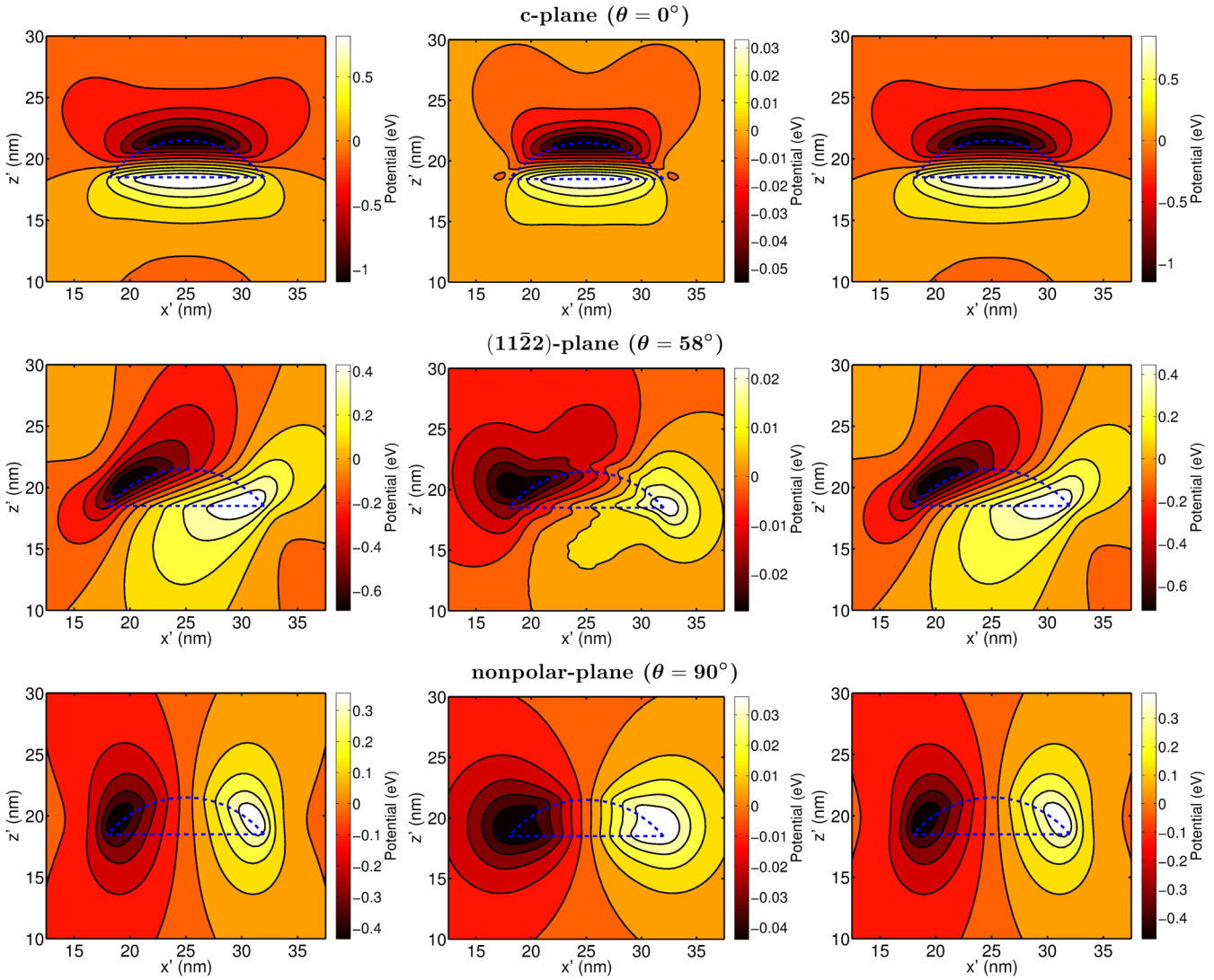

FIG. 3. Contour plots of the electrostatic built-in potential of lens-shaped GaN/AlN QDs grown on c (upper row), $(11\bar{2}2)$ (middle row), and nonpolar a planes (lower row). The contour plots are shown for a slice through the center of the QD in the x'-z' plane where the z' axis is parallel to the different growth directions considered here. (a) Built-in potential stemming from first-order piezoelectricity and spontaneous polarization. (b) Built-in potential arising from second-order piezoelectricity only. (c) Total built-in potential, originating from spontaneous polarization and first- and second-order piezoelectricity.

first-order piezoelectric polarization response. The second-order piezoelectric contribution is at least a factor of order 10 smaller. This finding is independent of the growth plane. Thus our calculations indicate that for GaN/AlN dots, second-order piezoelectric effects are of secondary importance for the total built-in potential. This is confirmed by the fact that the total built-in potential displayed in Fig. 3(c) is basically unchanged in comparison to Fig. 3(a), where second-order piezoelectric effects are absent.

Even though our results signal that second-order piezoelectric effects are small in GaN/AlN QDs, it should be noted that independently of the growth plane, this contribution is of the same symmetry as the combined response of first-order piezoelectric and spontaneous polarization. Therefore, if the second-order piezoelectric response were larger, an increase in the total built-in potential would be expected when accounting for these effects. This is in contrast to the situation in InGaAs/GaAs QDs, where first- and second-order piezoelectric contributions are opposite in sign [6]. This effect might even lead to a complete cancellation of first- and second-order built-in potentials and consequently to a field-free situation [6]. We find a similar situation for InGaN/GaN QDs grown on certain crystallographic planes, as we show in the following section. Also, we will discuss in more detail the origin of the observation that the second-order piezoelectric effect for the here studied GaN/AlN dots is of secondary importance and how this compares to InGaN/GaN systems.

2. *Built-in potentials in InGaN/GaN QDs grown on different substrate orientations*

Following the GaN/AlN QD analysis, Fig. 4 displays the electrostatic built-in potential for lens-shaped

$In_{0.2}Ga_{0.8}N$/GaN QDs grown along the c ($\theta = 0°$, upper row), the [11$\bar{2}$2] ($\theta = 58°$, middle row), and the nonpolar a axis ($\theta = 90°$, lower row). The QD geometry is indicated by the (white) dashed lines. The contour plots are again shown for a slice through the center of the dot in the x'-z' plane, where the z' axis is parallel to the respective growth axes. The left column, Fig. 4(a), depicts the "standard" calculation accounting for first-order piezoelectricity and spontaneous polarization but not second-order piezoelectricity. The middle column, Fig. 4(b), shows the second-order contribution only (no first-order piezoelectric and no spontaneous polarization) for the respective systems. The results of the full calculation, accounting for first- and second-order piezoelectricity as well as spontaneous polarization, are displayed in the right column, Fig. 4(c).

Similarly to the GaN/AlN QD data, when looking at Fig. 4(a) first, the semi- ($\theta = 58°$) and nonpolar ($\theta = 90°$) systems exhibit a strongly reduced built-in potential compared to the c-plane structure ($\theta = 0°$). In the c-plane system, the upper part of Fig. 4(a), the potential drop occurs along the growth direction. In the semipolar case the built-in potential exhibits an extremely complicated profile. For the nonpolar structure we observe a potential drop along the x' axis, which is parallel to the wurtzite c axis. It should be noted that in the nonpolar system, even though the built-in potential is not zero, the maxima and minima are located *outside* the nanostructure. Thus inside the QD the built-in potential is almost zero, resulting in a strong electron and hole wave function overlap in contrast to a c-plane system, as shown for instance in Ref. [88]. Furthermore, the potential profiles and magnitudes of the built-in potential are also different from the GaN/AlN dot systems studied in Fig. 3. We attribute this in part to the fact that the spontaneous polarization response

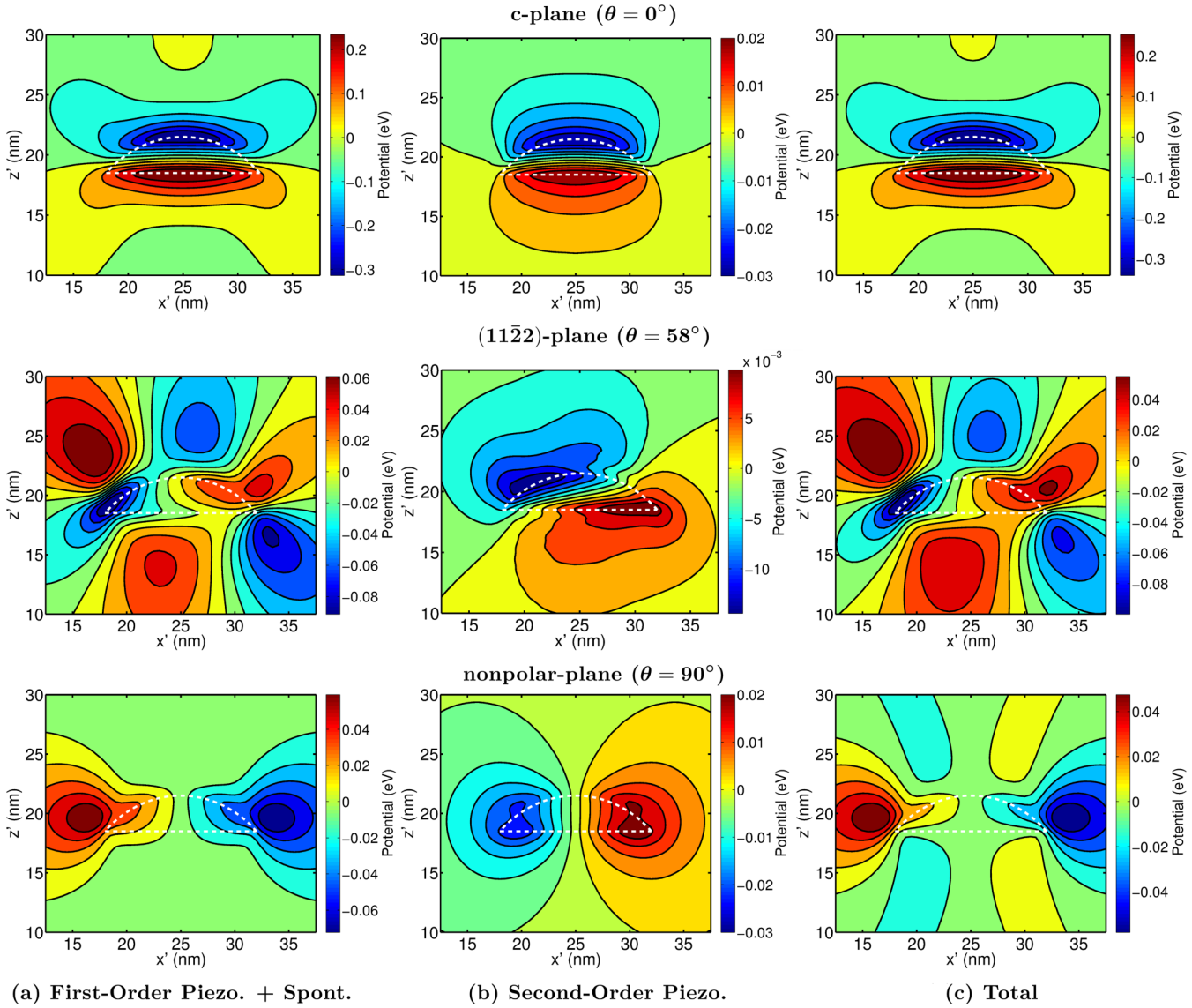

FIG. 4. Contour plots of the electrostatic built-in potential of lens-shaped $In_{0.2}Ga_{0.8}N$/GaN QDs grown on c (upper row), (11$\bar{2}$2) (middle row), and nonpolar planes (lower row). The contour plots are shown for a slice through the center of the QD in the x'-z' plane where the z' axis is parallel to the different growth directions considered here. (a) Built-in potential stemming from first-order piezoelectricity and spontaneous polarization. (b) Built-in potential arising from second-order piezoelectricity only. (c) Total built-in potential, originating from spontaneous polarization and first- and second-order piezoelectricity.

for InGaN/GaN systems is much smaller when compared to GaN/AlN [35,89]. While in GaN/AlN systems the spontaneous polarization contributes approximately 50% to the total built-in potential, in InGaN/GaN systems it is mainly dominated by the strain-dependent piezoelectric contributions [35,89]. We come back to this point again below.

We now turn to discussing second-order piezoelectric effects. Comparing the upper parts of Figs. 4(a) and 4(b) for the *c*-plane $In_{0.2}Ga_{0.8}N$/GaN dot system first, we find that the second-order piezoelectric contribution is significantly smaller than the potential arising from the combination of first-order piezoelectricity and spontaneous polarization. Again please note the different potential scales. Thus for the here considered *c*-plane system with 20% In the second-order contribution is of secondary importance. This is also confirmed by the result of the full calculation shown in Fig. 4(c), top panel. However, it is important to stress here that with increasing In content in *c*-plane InGaN/GaN QDs the second-order piezoelectric effect becomes significant. A detailed analysis of the built-in potential in *c*-plane InGaN/GaN QDs shows that for In contents $\geqslant$30%, second-order piezoelectric effects are important for an accurate description of the electronic and optical properties of these systems [40].

Turning to the QD structure grown on the $(11\bar{2}2)$ plane, Fig. 4(b), we find that the second-order piezoelectric effect is still noticeably smaller than the combined first-order piezoelectric and spontaneous polarization contribution, cf. Fig. 4(a), middle row. For the here considered lens-shaped $In_{0.2}Ga_{0.8}N$/GaN QD system the second-order piezoelectric contribution is a factor of order 5 smaller. Again it should be noted that for larger In contents, similarly to the *c*-plane system, stronger second-order contributions are expected. So further studies on these systems with different In contents shall be targeted in future work. Also, and this is in contrast to the GaN/AlN QD system, the built-in potential stemming from first-order piezoelectric and spontaneous polarization has a slightly different symmetry than the second-order piezoelectric contribution. This affects the overall built-in potential, cf. Fig. 4(c) (middle row), both in and around the QD. Thus, our results here give already first indications that a more complicated interplay of first- and second-order piezoelectric effects in InGaN/GaN QDs grown on semipolar planes could be expected especially for higher In contents and for different QD geometries.

The effect of built-in potential profile changes due to second-order piezoelectricity is even more pronounced for the nonpolar case, cf. Fig. 4 (lower row). When comparing Figs. 4(a) and 4(b) for the nonpolar system, we observe that the built-in potential arising from spontaneous and first-order piezoelectric polarization [Fig. 4(a)] has a similar symmetry to the second-order piezoelectric contribution [Fig. 4(b)]. However, and in contrast to Fig. 4(a) where the maxima and minima are located *outside* the nanostructure, the second-order piezoelectric contribution has its maxima and minima near the interfaces *inside* the dot. Furthermore, and most importantly, we find that inside the dot the magnitude of the built-in potential due to second-order piezoelectricity is comparable to the magnitude of the built-in potential stemming from spontaneous polarization and first-order piezoelectricity, but these contributions are opposite in sign. Consequently, the magnitude of the resulting total built-in potential is reduced compared to a situation where only first-order piezoelectricity and spontaneous polarization are accounted for. The total built-in potential is shown in Fig. 4(c). Thus, for the here considered nonpolar lens-shaped $In_{0.2}Ga_{0.8}N$/GaN QD not only the built-in potential magnitude is reduced; also the potential profile is modified both in and around the nanostructure.

In summary, we find here that for the considered semi- and nonpolar QD systems the second-order piezoelectric contribution is of secondary importance for GaN/AlN. This is in contrast to the InGaN/GaN system, even though the same QD geometry and approximately the same lattice mismatch have been chosen ($\epsilon^{In_{0.2}Ga_{0.8}N/GaN} \approx 2.2\%$, $\epsilon^{GaN/AlN} \approx 2.4\%$). The observed difference in the significance of the second-order piezoelectric effect originates mainly from the importance/unimportance of the spontaneous polarization in both systems as mentioned already above. In the semi- and nonpolar GaN/AlN system the overall built-in potential is basically dominated by the spontaneous polarization contribution (not shown here); this contribution is of secondary importance for the InGaN/GaN systems. This effect is already visible in the values of the spontaneous polarization of the respective binary materials (cf. Table I), keeping in mind that *differences* in the spontaneous polarization values determine mainly the corresponding built-in potential in a heterostructure. In connection to this, the spontaneous polarization component has a very simple dependence on the growth plane, cf. Eq. (A4), at least when compared to first-order and second-order piezoelectric contributions. These piezoelectric contributions exhibit a far more complicated behavior due to their strain dependence; cf. Eqs. (A1)–(A3) and (A5)–(A7). Thus the considered GaN/AlN QDs are dominated by spontaneous polarization effects while in InGaN/GaN dots a complex interplay of first-order, second-order, and spontaneous polarization contributions is observed, particularly for semi- and nonpolar QDs. Consequently, given that with increasing In content the second-order piezoelectric effect is expected to become even more important in InGaN/GaN QDs, these contributions should be taken into account for an accurate description of the electronic and optical properties of these systems.

In addition to the In content, also the QD geometry, as observed in zinc-blende InGaAs/GaAs dots [9], is expected to affect the magnitude and symmetry of the different piezoelectric contributions. We discussed already in Sec. II A that in the second-order piezoelectric polarization vector field several terms are linked to shear strain components. In QD systems these components become particularly large at sharp interfaces. For example in (truncated) hexagonal pyramids larger shear strain components are expected in comparison to lens-shaped QDs. Also dot anisotropies might lead to a further increase or decrease in the built-in-field-connected second-order piezoelectric effects when compared to fields in highly symmetric structure, e.g., elongated truncated pyramid vs hexagonal truncated pyramid. However, from an experimental viewpoint it presents an extremely challenging task to gain detailed insight into the dot geometry, especially after the nanostructures are capped with barrier material [90]. Nevertheless, for GaN/AlN QDs several studies reported truncated hexagonal pyramids for polar *c*-plane systems [91], while for

semi- and nonpolar planes rectangle-based truncated pyramids or arrowhead-shaped geometries with different facet incline angles have been outlined [49,50,80]. Unfortunately, far less information is given for InGaN-based systems, especially for non- and semipolar planes. Recent reports on *c*-plane InGaN/GaN QDs indicate that lens-shaped structures could be reasonable approximations [92,93]. For nonpolar QDs similar assumptions have been made in the theoretical modeling of these systems [81,82]. However, there is no detailed experimental information on the dot geometries of non- and semipolar InGaN QDs after *capping* with GaN.

Overall, to gain further insight into the importance of second-order piezoelectric effects for nitride-based QDs grown along different crystallographic directions a detailed theory-experiment comparison is desirable. However, and in contrast to QWs where calculated and measured built-in fields can directly be compared, cf. Table II, the situation is more complicated for dots. Here quantities such as transition energies, biexcitonic properties (binding and antibinding states), or radiative lifetimes are obvious candidates to further study second-order piezoelectricity. But these investigations require full electronic structure calculations and especially for semi- and nonpolar structures they should be combined with many-body approaches or at least Coulomb corrections. This originates from the fact that Coulomb effects can, for instance, compensate the spatial separation of the carriers due to the presence of residual built-in fields and affect the binding/antibinding character of biexcitons [81,88,94,95]. Such calculations, given the uncertainty of the InGaN/GaN QD geometry for non- and semipolar planes as discussed above, would have to be performed as a function of dot geometry. In general, future studies should therefore target a detailed analysis of the impact of increasing In content and variations in the QD geometry for different growth planes on the electrostatic built-in field and finally the electronic and optical properties of nitride-based QDs. However, such an analysis is beyond the scope of the present study since it requires also a careful choice of the electronic structure approach.

Nevertheless, it should be noted that our studies of the built-in field/potential for *c*-plane InGaN/GaN QD structures presented here are consistent with a recent combined theoretical and experimental study. Barettin *et al.* [92,93] studied electronic, optical, and transport properties of an array of InGaN/GaN QDs. The structural properties of these systems are characterized by dark-field transmission electron microscopy (TEM) and high-resolution TEM (HRTEM). The In contents observed in these systems [92,93] are between 16% to 23%, thus close to the here assumed 20% In. Furthermore, the HRTEM images indicate that a lens-shaped geometry is a reasonable approximation of the structures. Using this information, plus knowledge about the strain state of the system, Barettin and co-workers [92,93] performed $\mathbf{k}\cdot\mathbf{p}$-based calculations, including spontaneous and first-order piezoelectricity only. Within this framework they obtained very good agreement between theory and experiment for optical and transport properties. This finding is consistent with our results presented here in the sense that we observe for a lens-shaped *c*-plane InGaN/GaN QD with 20% In a very small second-order contribution (cf. Fig. 4). Thus for systems studied in Refs. [92,93] a first-order piezoelectricity model is already sufficient. However, for higher In contents, as for instance reported in Ref. [34], this could no longer be sufficient as already indicated in Ref. [40].

IV. CONCLUSION

In summary, we have presented a detailed analysis of second-order piezoelectric effects in wurtzite nitride-based heterostructures grown along different crystallographic directions. To accomplish this task, we have derived analytic expressions for the full second-order piezoelectric polarization vector field as a function of the incline angle θ to the wurtzite *c* axis. Even though our approach is applied to wurtzite III-N systems, it can also be applied to other wurtzite semiconductor systems such as ZnO once second-order piezoelectric coefficients are known.

Our calculations on III-N QW systems revealed that especially for semipolar growth planes with a high incline angle value ($55^\circ \leqslant \theta \leqslant 85^\circ$ and $105^\circ \leqslant \theta \leqslant 120^\circ$), second-order piezoelectric effects noticeably affect the built-in potential and thus the resulting electric field. More specifically, in an $In_{0.22}Ga_{0.78}N$/GaN MQW system, grown along the $[11\bar{2}2]$ direction, the electric field is increased by approximately 20% due to second-order piezoelectricity. Overall, we find that when including second-order piezoelectric effects in the theoretical framework, electric fields calculated for realistic MQW systems show a much better agreement with experimentally reported values. This further emphasizes the importance of second-order piezoelectric contributions for an accurate description of electrostatic built-in fields in nitride-based QWs.

Additionally, we have studied the electrostatic built-in potentials in lens-shaped GaN/AlN and $In_{0.2}Ga_{0.8}N$/GaN QDs grown on different substrate orientations, namely the *c*, the $(11\bar{2}2)$, and the nonpolar *a* plane. Our calculations reveal that, at least for the here chosen QD geometry, second-order piezoelectric contributions have a very small effect on the overall built-in potential in GaN/AlN systems. For the InGaN/GaN dot systems studied here the situation is different. While for a *c*-plane InGaN/GaN QD with 20% In the second-order contribution is of secondary importance, the situation is changed in the semi- and nonpolar systems. For example, in the nonpolar case, where the built-in potential is significantly reduced compared to the same *c*-plane structure, first- and second-order piezoelectric contributions are comparable in magnitude inside the dot. Moreover, the first- and second-order contributions are similar in symmetry but opposite in sign so that cancellation effects occur. This results also in changes in the built-in potential profile in and around the nanostructure. We relate the observed difference in the importance of second-order piezoelectricity in GaN/AlN and InGaN/GaN dot systems to the magnitude of the spontaneous polarization induced built-in potential. In GaN/AlN systems this component is large, at least when compared to InGaN/GaN systems.

Thus, based on all these studies, a complex interplay of first- and second-order piezoelectricity for InGaN-based QDs grown on different substrate orientations with varying In contents and dot geometries can be expected. Further studies shall focus on this in more detail and connect it to electronic and optical properties of the systems under consideration. This allows then for a detailed comparison with experiment.

ACKNOWLEDGMENTS

This work was supported by Science Foundation Ireland (Project No. 13/SIRG/2210). The authors would like to thank Miguel A. Caro and Eoin P. O'Reilly for fruitful discussions.

APPENDIX

In this Appendix we summarize the analytic expressions for first- and second-order piezoelectric polarization vector fields derived from the approach presented in Sec. II A. Please note that the expression for the first-order piezoelectric polarization vector can also be found in our previous work [45], which are similar to the expressions given in Ref. [29]. The equations for the rotated elastic tensor are explicitly given in Ref. [45] and are not repeated here.

1. First-order piezoelectric and spontaneous polarization vector field as a function of the incline angle θ

Using Eqs. (9) and (11), the x, y, and z components of the first-order piezoelectric polarization vector field, as a function of θ, are given by

$$P^{\mathrm{FO}}_{\mathrm{pz},x'} = \epsilon_{x'x'}\left[e_{33}\sin^3\theta + \left(\frac{e_{31}-2e_{15}}{2}\right)\sin(2\theta)\cos\theta\right] + \epsilon_{z'z'}\left[e_{31}\sin^3\theta + \left(\frac{e_{31}+2e_{15}}{2}\right)\sin(2\theta)\cos\theta\right] + \epsilon_{y'y'}[e_{31}\sin\theta] + \epsilon_{x'z'}[2e_{15}\cos(2\theta)\cos\theta - e_{33}\sin(2\theta)\sin\theta], \tag{A1}$$

$$P^{\mathrm{FO}}_{\mathrm{pz},y'} = 2e_{15}[\epsilon_{y'z'}\cos\theta - \epsilon_{x'y'}\sin\theta], \tag{A2}$$

$$P^{\mathrm{FO}}_{\mathrm{pz},z'} = \epsilon_{x'x'}\left[e_{31}\cos^3\theta + \left(\frac{e_{33}-2e_{15}}{2}\right)\sin(2\theta)\sin\theta\right] + \epsilon_{z'z'}\left[e_{33}\cos^3\theta + \left(\frac{e_{31}+2e_{15}}{2}\right)\sin(2\theta)\sin\theta\right] + \epsilon_{y'y'}[e_{31}\cos\theta] + \epsilon_{x'z'}[(e_{31}-e_{33})\sin(2\theta)\cos\theta + 2e_{15}\cos(2\theta)\sin\theta]. \tag{A3}$$

The required strain tensor components in the rotated frame are denoted by $\epsilon_{i'j'}$. For QW systems analytic expressions for $\epsilon_{i'j'}$ can be derived and are for instance given in Ref. [29].

For the spontaneous polarization $\mathbf{P}_{\mathrm{SP}}$ we find [45]

$$\mathbf{P}_{\mathrm{SP}} = \begin{pmatrix} -P_{sp}\sin\theta \\ 0 \\ P_{sp}\cos\theta \end{pmatrix}. \tag{A4}$$

2. Second-order piezoelectric polarization vector field as a function of the incline angle θ

Using the transformation rules described in Sec. II A, the x, y, and z components of the second-order piezoelectric polarization vector field as a function of incline angle θ read

$$P^{\mathrm{SO}}_{\mathrm{pz},x'} = 2B_{115}\cos\theta[A - BC] - 2B_{135}\cos\theta(FC) - 2B_{125}\cos\theta[A + \epsilon_{y'y'}C] - \frac{B_{311}}{2}\sin\theta\left[B^2 + 2D^2 + \epsilon^2_{y'y'}\right] + B_{312}\sin\theta[D^2 - \epsilon_{y'y'}B] - B_{313}\sin\theta[BF + \epsilon_{y'y'}F] - 2B_{344}\sin\theta[E^2 + C^2] - \frac{1}{2}\sin\theta B_{333}F^2, \tag{A5}$$

$$P^{\mathrm{SO}}_{\mathrm{pz},y'} = 2B_{115}[\epsilon_{y'y'}E - DC] + 2B_{135}EF + 2B_{125}[DC + EB], \tag{A6}$$

$$P^{\mathrm{SO}}_{\mathrm{pz},z'} = 2B_{115}\sin\theta[A - BC] - 2B_{135}\sin\theta[FC] - 2B_{125}\sin\theta[A + \epsilon_{y'y'}C] + \frac{B_{311}}{2}\cos\theta\left[B^2 + 2D^2 + \epsilon^2_{y'y'}\right] - B_{312}\cos\theta[D^2 - \epsilon_{y'y'}B] + B_{313}\cos\theta[BF + \epsilon_{y'y'}F] + 2B_{344}\cos\theta[E^2 + C^2] + \frac{1}{2}\cos\theta B_{333}F^2, \tag{A7}$$

where the coefficients $A, \ldots, F$ are given by

$$A = [\epsilon_{x'y'}\cos\theta + \epsilon_{y'z'}\sin\theta][\epsilon_{y'z'}\cos\theta - \epsilon_{x'y'}\sin\theta],$$
$$B = \epsilon_{x'x'}\cos^2\theta + \epsilon_{z'z'}\sin^2\theta + \epsilon_{x'z'}\sin(2\theta),$$
$$C = \left[\frac{\epsilon_{x'x'} - \epsilon_{z'z'}}{2}\right]\sin(2\theta) - \epsilon_{x'z'}\cos(2\theta),$$
$$D = \epsilon_{x'y'}\cos\theta + \epsilon_{y'z'}\sin\theta,$$
$$E = \epsilon_{y'z'}\cos\theta - \epsilon_{x'y'}\sin\theta,$$
$$F = \epsilon_{x'x'}\sin^2\theta + \epsilon_{z'z'}\cos^2\theta - \epsilon_{x'z'}\sin(2\theta).$$

[1] F. Bernardini, V. Fiorentini, and D. Vanderbilt, Phys. Rev. B **56**, R10024 (1997).
[2] F. Bernardini and V. Fiorentini, Phys. Rev. B **58**, 15292 (1998).
[3] O. Ambacher, J. Smart, J. R. Shealy, N. G. Weimann, K. Chu, M. Murphy, W. J. Schaff, L. F. Eastman, R. Dimitrov, L. Wittmer *et al.*, J. Appl. Phys. **85**, 3222 (1999).
[4] G. Bester and A. Zunger, Phys. Rev. B **71**, 045318 (2005).
[5] Z. L. Wang, Mater. Today **7**, 26 (2004).
[6] G. Bester, A. Zunger, X. Wu, and D. Vanderbilt, Phys. Rev. B **74**, 081305 (2006).
[7] G. Bester, X. Wu, D. Vanderbilt, and A. Zunger, Phys. Rev. Lett. **96**, 187602 (2006).
[8] H. Grimmer, Acta Crystallogr., Sect. A **63**, 441 (2007).
[9] A. Schliwa, M. Winkelnkemper, and D. Bimberg, Phys. Rev. B **76**, 205324 (2007).
[10] A. Beya-Wakata, P.-Y. Prodhomme, and G. Bester, Phys. Rev. B **84**, 195207 (2011).
[11] J. Pal, G. Tse, V. Haxha, M. A. Migliorato, and S. Tomić, Phys. Rev. B **84**, 085211 (2011).
[12] L. Pedesseau, C. Katan, and J. Even, Appl. Phys. Lett. **100**, 031903 (2012).
[13] R. Agrawal and H. D. Espinosa, Nano Lett. **11**, 786 (2011).
[14] M. S. Miao, Q. Yan, C. G. Van de Walle, W. K. Lou, L. L. Li, and K. Chang, Phys. Rev. Lett. **109**, 186803 (2012).
[15] M. A. Caro, S. Schulz, and E. P. O'Reilly, Phys. Rev. B **91**, 075203 (2015).
[16] G. Hu, W. Guo, R. Yu, X. Yang, R. Zhou, C. Pan, and Z. L. Wang, Nano Energy **23**, 27 (2016).
[17] S. Nakamura, M. Senoh, N. Iwasa, and S. Nagahama, Appl. Phys. Lett. **67**, 1868 (1995).
[18] E. Kuokstis, C. Q. Chen, M. E. Gaevski, W. H. Sun, J. W. Yang, G. Simin, M. A. Khan, H. P. Maruska, D. W. Hill, M. C. Chou *et al.*, Appl. Phys. Lett. **81**, 4130 (2002).
[19] N. Grandjean, B. Damilano, S. Dalmasso, M. Leroux, M. Laügt, and J. Massies, J. Appl. Phys. **86**, 3714 (1999).
[20] O. Ambacher, J. Majewski, C. Miskys, A. Link, M. Hermann, M. Eickhoff, M. Stutzmann, F. Bernardini, V. Fiorentini, V. Tilak *et al.*, J. Phys.: Condens. Matter **14**, 3399 (2002).
[21] H. Masui, J. Sonoda, N. Pfaff, I. Koslow, S. Nakamura, and S. P. DenBaars, J. Phys. D: Appl. Phys. **41**, 165105 (2008).
[22] S. P. DenBaars, D. Feezell, K. Kelchner, S. Pimputkar, C.-C. Pan, C.-C. Yen, S. Tanaka, Y. Zhao, N. Pfaff, R. Farrell *et al.*, Acta Mater. **61**, 945 (2013).
[23] J. S. Im, H. Kollmer, J. Off, A. Sohmer, F. Scholz, and A. Hangleiter, Phys. Rev. B **57**, R9435 (1998).
[24] A. D. Andreev and E. P. O'Reilly, Appl. Phys. Lett. **79**, 521 (2001).
[25] S. K. Patra, T. Wang, T. J. Puchtler, T. Zhu, R. A. Oliver, R. A. Taylor, and S. Schulz, Phys. Status Solidi B **254**, 1600675 (2017).
[26] M. Albrecht, H. P. Strunk, J. L. Weyher, I. Grzegory, S. Porowski, and T. Wosinski, J. Appl. Phys. **92**, 2000 (2002).
[27] W. Li, S. Sharmin, H. Ilatikhameneh, R. Rahman, Y. Lu, J. Wang, X. Yan, A. Seabaugh, G. Klimeck, D. Jena *et al.*, IEEE J. Exploratory Solid-State Comput. Devices Circuits **1**, 28 (2015).
[28] T. A. Ameen, H. Ilatikhameneh, J. Z. Huang, M. Povolotsky, R. Rahman, and G. Klimeck, IEEE Trans. Electron Devices **64**, 2512 (2017).
[29] A. E. Romanov, T. J. Baker, S. Nakamura, and J. S. Speck, J. Appl. Phys. **100**, 023522 (2006).
[30] U. T. Schwarz and M. Kneissl, Phys. Status Solidi RRL **1**, A44 (2007).
[31] D. Jena, J. Simon, A. Wang, Y. Cao, K. Goodman, J. Verma, S. Ganguly, G. Li, K. Karda, V. Protasenko *et al.*, Phys. Status Solidi A **208**, 1511 (2011).
[32] M. A. Caro, S. Schulz, S. B. Healy, and E. P. O'Reilly, J. Appl. Phys. **109**, 084110 (2011).
[33] S. Schulz and E. P. O'Reilly, Phys. Rev. B **82**, 033411 (2010).
[34] T. Frost, A. Hazari, A. Aiello, M. Z. Baten, L. Yan, J. Mirecki-Millunchick, and P. Bhattacharya, Jpn. J. Appl. Phys. **55**, 032101 (2016).
[35] C. X. Ren, Mater. Sci. Technol. **32**, 418 (2016).
[36] G. M. O. Hönig, S. Westerkamp, A. Hoffmann, and G. Callsen, Phys. Rev. Appl. **7**, 024004 (2017).
[37] O. Stier, M. Grundmann, and D. Bimberg, Phys. Rev. B **59**, 5688 (1999).
[38] P.-Y. Prodhomme, A. Beya-Wakata, and G. Bester, Phys. Rev. B **88**, 121304 (2013).
[39] M. A. Migliorato, J. Pal, R. Garg, G. Tse, H. Y. Al-Zahrani, U. Monteverde, S. Tomić, C.-K. Li, Y.-R. Wu, B. G. Crutchley *et al.*, AIP Conf. Proc. **1590**, 32 (2014).
[40] S. K. Patra and S. Schulz, Appl. Phys. Lett. **111**, 103103 (2017).
[41] J. F. Nye, *Physical Properties of Crystals: Their Representation by Tensors and Matrices* (Oxford University Press, New York, 1985).
[42] A. D. Andreev and E. P. O'Reilly, Phys. Rev. B **62**, 15851 (2000).
[43] O. Marquardt, T. Hickel, and J. Neugebauer, J. Appl. Phys. **106**, 083707 (2009).
[44] A. Schliwa, G. Hönig, and D. Bimberg, in *Electronic Properties of III-V Quantum Dots* (Springer International Publishing, Cham, 2014), pp. 57–85.
[45] S. Schulz and O. Marquardt, Phys. Rev. Appl. **3**, 064020 (2015).
[46] D. F. Feezell, J. S. Speck, S. P. DenBaars, and S. Nakamura, J. Display Technol. **9**, 190 (2013).
[47] M. Funato, M. Ueda, D. Inoue, Y. Kawakami, Y. Narukawa, and T. Mukai, Appl. Phys. Express **3**, 071001 (2010).
[48] J. Brault, D. Rosales, B. Damilano, M. Leroux, A. Courville, M. Korytov, S. Chenot, P. Vennéguès, B. Vinter, P. D. Mierry *et al.*, Semicond. Sci. Technol. **29**, 084001 (2014).
[49] G. P. Dimitrakopulos, E. Kalesaki, J. Kioseoglou, T. Kehagias, A. Lotsari, L. Lahourcade, E. Monroy, I. Heusler, H. Kirmse, W. Neumann *et al.*, J. Appl. Phys. **108**, 104304 (2010).
[50] G. Zhao, L. Wang, S. Yang, H. Li, H. Wei, D. Han, and Z. Wang, Sci. Rep. **6**, 20787 (2016).
[51] H. Masui, S. Nakamura, S. P. DenBaars, and U. K. Mishra, IEEE Trans. Electron Devices **57**, 88 (2010).
[52] S. Schulz, M. A. Caro, E. P. O'Reilly, and O. Marquardt, Phys. Rev. B **84**, 125312 (2011).
[53] J.-H. Kang, M. Galicka, P. Kacman, and H. Shtrikman, Nano Lett. **17**, 531 (2017).
[54] C. Stampfl and C. G. Van de Walle, Phys. Rev. B **57**, R15052 (1998).
[55] M. Grundmann, *The Physics of Semiconductors*, Graduate Texts in Physics (Springer, Berlin, 2010).
[56] I. Vurgaftman and J. R. Meyer, J. Appl. Phys. **94**, 3675 (2003).
[57] M. A. Caro, S. Schulz, and E. P. O'Reilly, Phys. Rev. B **86**, 014117 (2012).
[58] M. A. Caro, S. Schulz, and E. P. O'Reilly, Phys. Rev. B **88**, 214103 (2013).

[59] H. Morkoç, in *Electronic Band Structure and Polarization Effects* (Wiley-VCH, Weinheim, Germany, 2009), pp. 131–321.
[60] O. Marquardt, S. Boeck, C. Freysoldt, T. Hickel, and J. Neugebauer, Comput. Phys. Commun. **181**, 765 (2010).
[61] S. Boeck, C. Freysoldt, A. Dick, L. Ismer, and J. Neugebauer, Comput. Phys. Commun. **182**, 543 (2011).
[62] C. Pryor, J. Kim, L. W. Wang, A. J. Williamson, and A. Zunger, J. Appl. Phys. **83**, 2548 (1998).
[63] J. Wu, J. Appl. Phys. **106**, 011101 (2009).
[64] U. M. E. Christmas, A. D. Andreev, and D. A. Faux, J. Appl. Phys. **98**, 073522 (2005).
[65] S. K. Patra, O. Marquardt, and S. Schulz, Opt. Quantum Electron. **48**, 151 (2016).
[66] S. Muensit, E. M. Goldys, and I. L. Guy, Appl. Phys. Lett. **75**, 3965 (1999).
[67] F. Bernardini and V. Fiorentini, Appl. Phys. Lett. **80**, 4145 (2002).
[68] C. Adelmann, E. Sarigiannidou, D. Jalabert, Y. Hori, J.-L. Rouvière, B. Daudin, S. Fanget, C. Bru-Chevallier, T. Shibata, and M. Tanaka, Appl. Phys. Lett. **82**, 4154 (2003).
[69] A. Helman, M. Tchernycheva, A. Lusson, E. Warde, F. H. Julien, K. Moumanis, G. Fishman, E. Monroy, B. Daudin, D. L. S. Dang *et al.*, Appl. Phys. Lett. **83**, 5196 (2003).
[70] C. Buchheim, R. Goldhahn, A. T. Winzer, G. Gobsch, U. Rossow, D. Fuhrmann, A. Hangleiter, F. Furtmayr, and M. Eickhoff, Appl. Phys. Lett. **90**, 241906 (2007).
[71] A. Hangleiter, F. Hitzel, S. Lahmann, and U. Rossow, Appl. Phys. Lett. **83**, 1169 (2003).
[72] H. Shen, G. A. Garrett, M. Wraback, H. Zhong, A. Tyagi, S. P. DenBaars, S. Nakamura, and J. S. Speck, Phys. Status Solidi C **7**, 2378 (2010).
[73] A. Das, G. P. Dimitrakopulos, Y. Kotsar, A. Lotsari, T. Kehagias, P. Komninou, and E. Monroy, Appl. Phys. Lett. **98**, 201911 (2011).
[74] A. Das, P. Sinha, Y. Kotsar, P. Kandaswamy, G. Dimitrakopulos, T. Kehagias, P. Komninou, G. Nataf, P. D. Mierry, and E. Monroy, J. Cryst. Growth **323**, 161 (2011).
[75] T. Zhu, F. Oehler, B. P. L. Reid, R. M. Emery, R. A. Taylor, M. J. Kappers, and R. A. Oliver, Appl. Phys. Lett. **102**, 251905 (2013).
[76] T. Zhu, J. T. Griffiths, W. Y. Fu, A. Howkins, I. W. Boyd, M. J. Kappers, and R. A. Oliver, Superlatt. Microstruct. **88**, 480 (2015).
[77] X. Yang, M. Arita, S. Kako, and Y. Arakawa, Appl. Phys. Lett. **99**, 061914 (2011).
[78] T. Wang, T. J. Puchtler, S. K. Patra, T. Zhu, M. Ali, T. J. Badcock, T. Ding, R. A. Oliver, S. Schulz, and R. A. Taylor, Nanophotonics **6**, 1175 (2017).
[79] S. Founta, F. Rol, E. Bellet-Amalric, J. Bleuse, B. Daudin, B. Gayral, H. Mariette, and C. Moisson, Appl. Phys. Lett. **86**, 171901 (2005).
[80] S. Founta, C. Bougerol, H. Mariette, B. Daudin, and P. Vennéguès, J. Appl. Phys. **102**, 074304 (2007).
[81] S. Barthel, K. Schuh, O. Marquardt, T. Hickel, J. Neugebauer, F. Jahnke, and G. Czycholl, Eur. Phys. J. B **86**, 449 (2013).
[82] K. Schuh, S. Barthel, O. Marquardt, T. Hickel, J. Neugebauer, G. Czycholl, and F. Jahnke, Appl. Phys. Lett. **100**, 092103 (2012).
[83] T. Wang, T. J. Puchtler, S. K. Patra, T. Zhu, J. C. Jarman, R. A. Oliver, S. Schulz, and R. A. Taylor, Sci. Rep. **7**, 12067 (2017).
[84] M. Sénès, K. L. Smith, T. M. Smeeton, S. E. Hooper, and J. Heffernan, Phys. Rev. B **75**, 045314 (2007).
[85] A. F. Jarjour, R. A. Oliver, A. Tahraoui, M. J. Kappers, C. J. Humphreys, and R. A. Taylor, Phys. Rev. Lett. **99**, 197403 (2007).
[86] J. Simon, N. T. Pelekanos, C. Adelmann, E. Martinez-Guerrero, R. André, B. Daudin, L. S. Dang, and H. Mariette, Phys. Rev. B **68**, 035312 (2003).
[87] S. Schulz, A. Berube, and E. P. O'Reilly, Phys. Rev. B **79**, 081401 (2009).
[88] S. K. Patra and S. Schulz, J. Phys. D: Appl. Phys. **50**, 025108 (2017).
[89] D. P. Williams, A. D. Andreev, E. P. O'Reilly, and D. A. Faux, Phys. Rev. B **72**, 235318 (2005).
[90] F. Ferdos, S. Wang, Y. Wei, A. Larsson, M. Sadeghi, and Q. Zhao, Appl. Phys. Lett. **81**, 1195 (2002).
[91] M. Arlery, J. L. Rouviere, F. Widmann, B. Daudin, G. Feuillet, and H. Mariette, Appl. Phys. Lett. **74**, 3287 (1999).
[92] D. Barettin, M. A. der Maur, A. di Carlo, A. Pecchia, A. F. Tsatsulnikov, A. V. Sakharov, W. V. Lundin, A. E. Nikolaev, S. O. Usov, N. Cherkashin *et al.*, Nanotechnology **28**, 015701 (2017).
[93] D. Barettin, M. A. der Maur, A. di Carlo, A. Pecchia, A. F. Tsatsulnikov, W. V. Lundin, A. V. Sakharov, A. E. Nikolaev, M. Korytov, N. Cherkashin *et al.*, Nanotechnology **28**, 275201 (2017).
[94] S. Tomić and N. Vukmirović, Phys. Rev. B **79**, 245330 (2009).
[95] S. Schulz, M. A. Caro, and E. P. O'Reilly, Appl. Phys. Lett. **101**, 113107 (2012).